

Towards Robotic Eye Surgery: Marker-free, Online Hand-eye Calibration using Optical Coherence Tomography Images

Mingchuan Zhou*, Mahdi Hamad*, Jakob Weiss, Abouzar Eslami,
Kai Huang, Mathias Maier, Chris P. Lohmann, Nassir Navab, Alois Knoll, M. Ali Nasser

Abstract—Ophthalmic microsurgery is known to be a challenging operation, which requires very precise and dexterous manipulation. Image guided robot-assisted surgery (RAS) is a promising solution that brings significant improvements in outcomes and reduces the physical limitations of human surgeons. However, this technology must be further developed before it can be routinely used in clinics. One of the problems is the lack of proper calibration between the robotic manipulator and appropriate imaging device. In this work, we developed a flexible framework for hand-eye calibration of an ophthalmic robot with a microscope-integrated Optical Coherence Tomography (MI-OCT) without any markers. The proposed method consists of three main steps: a) we estimate the OCT calibration parameters; b) with micro-scale displacements controlled by the robot, we detect and segment the needle tip in 3D-OCT volume; c) we find the transformation between the coordinate system of the OCT camera and the coordinate system of the robot. We verified the capability of our framework in ex-vivo pig eye experiments and compared the results with a reference method (marker-based). In all experiments, our method showed a small difference from the marker based method, with a mean calibration error of 9.2 μm and 7.0 μm , respectively. Additionally, the noise test shows the robustness of the proposed method.

Index Terms—Computer vision for medical robotics, medical robots and systems, Optical Coherence Tomography, hand-eye calibration.

I. INTRODUCTION

OPHTHALMIC surgery is a typical microsurgery with a delicate and complex workflow, which needs critical surgical skills and considerations (Fig. 1). Due to this fact, the ophthalmologists are required not only to have enough training and clinical experiences but also need to be in a good physical condition to cope with hand tremors and a non-stop surgery session. However, for surgeons, clinical experience normally comes with age, but aging impairs physical skills. Recently,

Manuscript received: February, 24, 2018; Revised May, 11, 2018; Accepted July, 9, 2018. This paper was recommended for publication by Editor Francois Chaumette upon evaluation of the Associate Editor and Reviewers' comments.

*The first two authors contribute equally to this paper.

Mingchuan Zhou, Mahdi Hamad, and Alois Knoll are with Chair for Robotics and Embedded Systems, Technische Universität München, Germany. {zhoum, mahdi.hamad, knoll}@tum.de

Jakob Weiss and Nassir Navab are with Chair for Computer Aided Medical Procedures and Augmented Reality, Technische Universität München, Germany. {jakob.weiss, navab}@tum.de

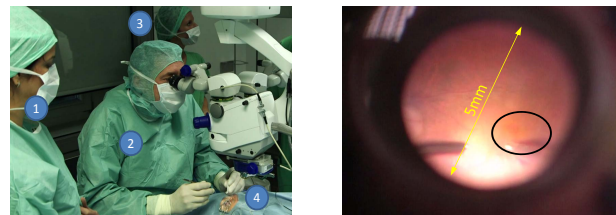
Abouzar Eslami is with Carl Zeiss Meditec, Germany. abouzar.eslami@zeiss.com

Kai Huang is with School of Data and Computer Science, Sun Yat-Sen University, China. huangk36@mail.sysu.edu.cn

Mathias Maier, Chris P. Lohmann, and M. Ali Nasser are with Augenklinik und Poliklinik, Klinikum rechts der Isar der Technische Universität München, Germany. {mathias.maier, chris.lohmann, ali.nasser}@mri.tum.de

Digital Object Identifier (DOI): 10.1109/LRA.2018.2858744

robot-assisted surgery (RAS) has been known as a solution for reducing the work intensity, increasing the surgical outcomes and prolonging the service time of experienced surgeons. To address the challenges of ophthalmic surgery, many researchers in the past decade introduced high precision robotic setups with different scales and design mechanisms [1]–[10]. Over the years, these robots are getting closer to clinical trials. In September 2016, surgeons at Oxford's John Radcliffe Hospital, performed the world's first robotic Internal Limiting Membrane (ILM) peeling, in which the surgeon removes one membrane from a specific area of the retina. The eye surgical robot named Robotic Retinal Dissection Device (R2D2) with 10 μm accuracy was used in the clinical trials [11] [12], which proved the feasibility of RAS application in one of the most difficult ophthalmic operations.



(a) Ophthalmic operation (b) Microscope view of focal region

Fig. 1. (a): A conventional setting in an ophthalmic operation room: a surgeon (2); two assistants (1) and (3); the patient (4). (b): The focal region in the microscopic view. The operation area is marked by an ellipse.

Furthermore, advances in ophthalmologic imaging modalities and sensing devices are always being introduced to the surgery, which, when integrated with robotic systems, will give surgeons more confidence to make reliable intra-operative decisions. In addition to conventional en-face images from the ophthalmic microscopes, Optical Coherence Tomography (OCT) is currently known to be a proper imaging modality for visualizing the micro structural anatomy of the eye [13], as it offers suitable resolution and non-invasive radiation. Compared to the stereo-microscope vision system proposed by Probst et al. [14], the drawbacks of OCT are expensive hardware, acquisition and processing time, while the advantages are (a) the imaging quality will not be influenced by the illumination, which in some cases (e.g. vitreoretinal surgery, an operation on the posterior segment of the eye) is not easy to control, and (b) the OCT can provide information inside the tissue, which allows surgeons to analyze the anatomical structures. The latest OCT machines have been developed to even give real-time information of the interior and posterior

segment of the eye as well as the interactions between surgical instruments and intraocular tissues [15].

Some research groups integrated the OCT probe into surgical instruments for navigation in head surgery [16] and ophthalmic surgery [17]. However, to localize the global location of a probe, this may need preoperative Computer Tomography (CT) or Magnetic Resonance Imaging (MRI). These extra preoperative images and modified surgical instruments may increase the complexity of the application.

Instead of using OCT integrated instruments, we propose using the microscope-integrated OCT (MI-OCT) for RAS navigation. In MI-OCT, the OCT engine is integrated inside the microscope head and shares the same optical path with the microscope in order to capture volumetric images, thus the OCT probe avoids integration into surgical instrument. During the planned MI-OCT guided RAS, the surgeon will move the microscope head and adjust its view to locate the focal region (Fig. 1(b)). Usually, the microscope imaging area is enough to cover the focal area, thus the microscope head could be fixed. Following this fixation, the surgeon will manipulate the robot and move the needle close to the focal area. Therefore, hand-eye calibration is essential for such applications e.g. keeping a safe distance between needle tip and retina or performing path planning for targeted drug delivery.

In this paper, we address the problem of hand-eye calibration for a surgical robot with the MI-OCT camera. For this purpose, we use a surgical robot developed by [18]. In this setup, head and eye fixations are used to reduce the risk of movement caused by the patient. The imaging device and the robot should also be rigidly connected to the operation bed following the configuration of a da Vinci surgical system. These setups are necessary for the RAS surgery and will usually require only a one-time calibration. To the best of our knowledge, this is the first paper that proposes such a calibration framework. The main contributions of this paper are summarized as follows:

- We propose a flexible framework for hand-eye calibration of an ophthalmic robot and OCT camera without using additional markers;
- A robust method for needle tip segmentation and localization in OCT volume is proposed;
- Clinical grade accuracy performance (9.2 μm) of the calibration method is demonstrated by experimental evaluations on ex-vivo pig eyes.

The remainder of the paper is organized as follows. In the next section, we briefly present related work. The proposed hand-eye calibration framework is described in Section II. In Section IV, the performance of the proposed method is evaluated. Experimental results are discussed in Section V. Finally, Section VI concludes this paper and presents the future work.

II. RELATED WORK

Hand-eye calibration is an active research topic in robotics and has been investigated by many researchers. In particular, the seminal work of Tsai et al. since 1980s [19]. There exist several off-the-shelf calibration solutions that implement Tsai's method (e.g. ViSP library [20], which is designed for visual servoing applications). These existing off-the-shelf calibration solutions can be easily integrated into standard

camera vision systems and allow fast prototyping. However, they require separate measurements and extra equipment (calibration grids, markers,...). In some medical scenarios, it is not practical to place the calibration objects or markers inside the tissue or bodily organ. In addition, medical imaging modalities (e.g. OCT and ultrasound) have different imaging principles, which leads to a different camera calibration process.

In the surgical environment, hand-eye calibration is normally transferred into a Procrustean problem by the [21] and has been modified to meet with different surgical requirements in various 3D medical imaging scenarios, e.g. two-camera stereoscopic vision and ultrasound. To determine the unknown fixed transformation between the robot and imaging coordinates, a ball-tip stylus or chessboard is used as a calibrator for hand-eye calibration [22]. However, these markers may influence the conventional surgical workflow as well as cause complication with sterility. Thompson et al. [23] designed a tracking collar for rigid laparoscopes hand-eye calibration. The method can achieve 0.85 mm error, and the calibration process can be finished within 3 minutes. In another work, 3D markers were used by Bergmeir et al. [24] to realize ultrasound probe calibration with a robotic arm. In terms of none marker research work, Sarrazin et al. [25] used ultrasound volume registration data to achieve calibration that does not require 3D localizers. Pachtrachai et al. [26] proposed a calibration method where an instrument with known geometry is used instead of an additional calibrator. The calibration was achieved without compromising sterility. Francisco et al. [27], [28] used constraints based on the needle orientation in 2D/3D ultrasound image to calibrate the ultrasound probe.

Taking the above research work and requirements of ophthalmic surgery into account, we can conclude that the following considerations need to be taken into account for a qualified calibration method: (a) external calibration objects are best avoided to reduce surgical complication; (b) small computational overhead can make the method easier for online implementation; (c) the calibration accuracy needs to be kept within clinical tolerance. Unlike the aforementioned surgical applications, the intended operation area for ophthalmic surgery is very small and the precision requirement is much higher. The precision requirement of ophthalmic surgery varies depending on the specific operation. For the ILM peeling process, the surgeon can do it quite well, which means the 182 μm accuracy (the hand tremor RMS amplitude [29]) is enough. For the sub-retinal injection, the average thickness of retina is around 200 μm , therefore, 20 μm would be an acceptable position accuracy. For the retinal vein cannulation, the ideal position accuracy would be 20 μm , since the diameter of branch retinal veins is typically less than 200 μm . Therefore, the typical position accuracy for robotic eye surgery is considered to be roughly around 10 μm [2], [7], [10] to meet all potential operations.

Due to the properties of microsurgeries, it will be complicated to properly place calibration markers during surgery, specifically for the posterior parts, where the markers could move inside the eye. To overcome the high accuracy requirement challenge, we propose using the robot's precise movement, in three orthogonal directions, and the detected needle tip position, to obtain the transformation matrix between the camera and the robot coordinate system.

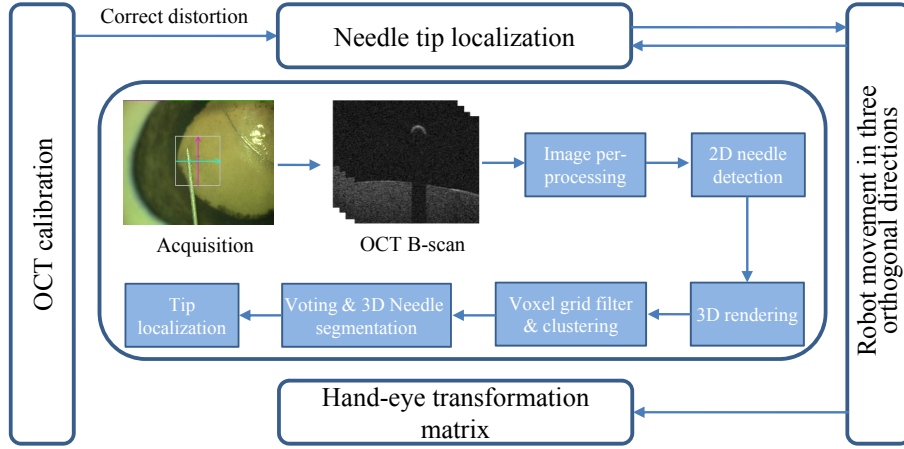


Fig. 2. The framework of the proposed method.

III. METHOD

The proposed framework is shown in Fig. 2. The OCT calibration parameters are obtained in advance to eliminate the distortion caused by the imaging device. With micro-scale displacements controlled by the robot, we move the needle in a trajectory that contains three orthogonal directions. Following each movement, an OCT volume is captured, and the needle tip is detected and accurately segmented even with the presence of image noise. After finishing all the movements defined by the trajectory, we calculate the transformation between the coordinate system of the OCT camera and the coordinate system of the robot. The details of each step are presented as follows.

A. OCT calibration

Our setup contains an OPMI LUMERA 700 with integrated RESCAN 700 OCT (Carl Zeiss Meditec AG., Germany). The OCT engine is spectral domain OCT, which has improved scanning speed compared to time domain OCT. The OCT engine has a wavelength of 840 nm and a scanning speed of 54000 A-scans per second. Due to the fact that the intended surgical area for ophthalmic operation is usually very small, we set the internal mirror galvanometer, which can deflect a light beam by an electric current, in the OCT to obtain the scan area $3.01 \text{ mm} \times 3.10 \text{ mm} \times 2.60 \text{ mm}$ with the highest resolution of 128 B-scans, each with 512 A-scans. B-scan refers to a two dimensional, cross-section scan and A-scan is one dimensional scan.

The simplified principle of an OCT scanner is shown in Fig. 3. The cross-sectional profiles of the flat surface is curved, because the two scan mirrors M_x and M_y have different scan radius which arch the beaming path. During the scanning in the X- and Y- direction, M_y and M_x are fixed, respectively. Therefore, there are geometric distortion effects imposed onto the OCT volume by two mirror galvanometers, which are considered to be decoupled from each other. We refer to the method which is proposed by Van der Jeught *et al.* [30] to correct the OCT distortion. The glass slider ($26 \text{ mm} \times 76 \text{ mm} \times 1 \text{ mm}$) with flatness error of $\pm 3 \mu\text{m}$ is used as the flat surface (Brand GmbH, Germany). The topmost surface of the mirror is recognized with the threshold filter in each

B-scan image. The radius of the topmost surface is fitted by the analytical equation of a circle, thereby the virtual pivot center (x_c, z_{xc}) of the mirror galvanometer is calculated by averaging all fitted circle centers for the B-scans in X-direction (B_x). We repeat the same process to obtain the virtual pivot center (y_c, z_{yc}) with all the B-scans in Y-direction (B_y). The distortion correction equation is reported below,

$$\begin{cases} x' = R_x(x, z) \sin(\theta(x, z)) + x_c \\ y' = R_y(y, z^*) \sin(\varphi(y, z^*)) + y_c \\ z' = R_y(y, z^*) \cos(\varphi(y, z^*)) + z_{yc} \end{cases} \quad (1)$$

where the point (x', y', z') is the corrected result of the point (x, y, z) in the original volume, $R_x(x, y)$ denotes the distance between virtual pivot center (x_c, z_{xc}) and (x, z) , $\sin(\theta(x, z))$ denotes the angle of polar coordinate system with the virtual pivot center of M_x , z^* which equals $R_x(x, z) \cos(\theta(x, z)) + z_{xc}$ is the corrected z value for the distortion causing from M_x scanning mirror, $R_y(y, z^*)$ denotes the distance between virtual pivot center (y_c, z_{yc}) and (y, z^*) , $\varphi(y, z^*)$ denotes the angle of the polar coordinate system with the virtual pivot center M_y .

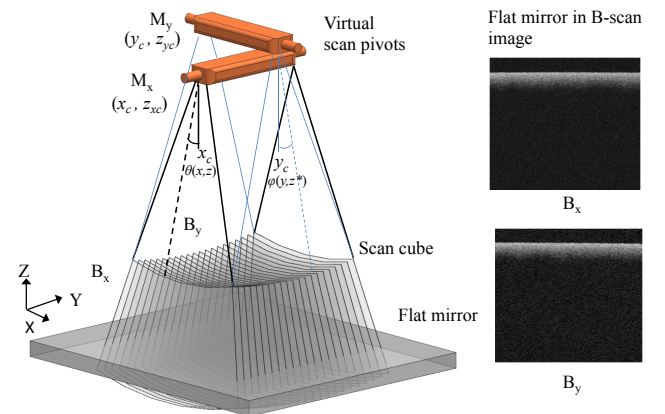


Fig. 3. The distortion of OCT scan and the cross-sectional B-scan images.

B. Needle tip localization

Instead of using 3D markers for hand-eye calibration, in our approach, we directly utilize a robust and precise method to localize the needle tip in OCT images. The actual tip is invisible due to the light diffraction and its optical property, therefore, this detected needle tip is the smallest tip part in the OCT images. The original B-scan gray image (Fig. 4(a)) is transformed into a binary image by the thresholding method. The threshold value is adaptively defined, based on the statistical measurements of each B-scan [31]. We eliminate the noise inside the binary image, by applying a median filter followed by a Gaussian filter. The sizes of the median and Gaussian filters are much less than the visible needle tip. Therefore, the smallest visible tip part will not be missed as a result of the de-noising procedure.

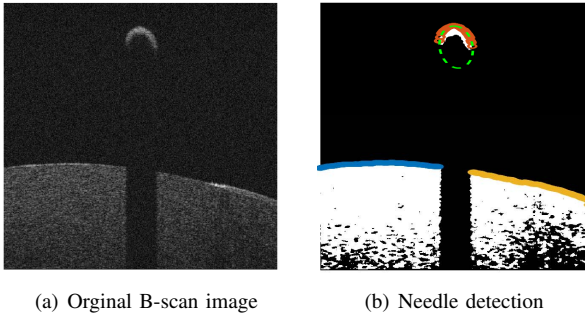


Fig. 4. The original B-scan image (a) and needle detection using ellipse fitting for topmost of contours (b). The ellipse with green dash line is the detected ellipse for needle body. The contours are marked with different colors for different connection areas.

A voting mechanism is used to specify whether a point in the 2D image belongs to the needle body. Since the needle body part in the B-scan image is a half ellipse, which can be considered as a strong feature, the ellipse fitting is applied to the topmost contours of each B-scan. The topmost contours are obtained by scanning each column of pixels going from top to bottom (Z-direction), starting from the leftmost column and moving to the right (X-direction). The connected contour pixels (blue, yellow, and red in Fig. 4(b)) are considered as one group and fitted to an ellipse equation. In order to filter any ellipse detected other than the needle body (e.g. blue&yellow eye tissue), we constrain the ellipse's minor axis to a value lower than m_e , where m_e is defined based on the diameter of the instrument (i.e. needle). The fitted ellipse is shown as a green color in Fig. 4(b). Finally, an additional property (Boolean value) is added to each pixel in B-scan. The Boolean value is true if the pixel belongs to the fitted ellipse. Otherwise, it is false.

In order to render the images in 3D, the OCT volume is represented as a point cloud structure \mathcal{P} (Fig. 5(a)) with (x_i, y_i, z_i, b_i) , where (x_i, y_i, z_i) is the position of point $p_i \in \mathcal{P}$, and b_i is the Boolean value to identify whether the point belongs to the needle. To reduce the excessive amounts of data and computation overhead, a voxel grid filter with a leaf size of 0.02 mm is used. Afterwards, we need to differentiate between objects in the point cloud. For this, we use Euclidean cluster extraction. The clustering step uses a Kd-tree structure for finding the nearest neighbors of every point in the cloud.

Two points p_i and p_j belong to two different clusters c_i and c_j if:

$$\min \| p_i - p_j \|_2 \geq t \quad (2)$$

where t is the maximum imposed distance threshold. The result of these processing steps (Fig. 5(b)) is a set of euclidean point clusters $C = \{(c_1) \dots (c_n)\}$, where each segmented cluster c_i is at least t far away from the other cluster. At this point, we have two different clusters, but we do not know which one is the needle. To segment the needle (see Algorithm 1), the cluster that has the greatest number of points with $b_i = 1$ (i.e. most voting, blue color in Fig. 5(c)) will be treated as the needle (Fig. 5(d)). In order to localize the needle tip, the B-scan direction can be adjusted manually or automatically to match with the needle insertion direction [31]. The alignment will not add extra complexity since it only costs several seconds manually with the scanner control panel of RESCAN 700 OCT. As a result, the needle tip will always be located in the first B-scan (slice) of the segmented needle. The yellow point (Fig. 5(d)) is the centroid of the needle cluster in this slice, which represents the needle tip. Finally, the needle tip position is calibrated by Eqn. 1 to correct for the distortion in the OCT volume.

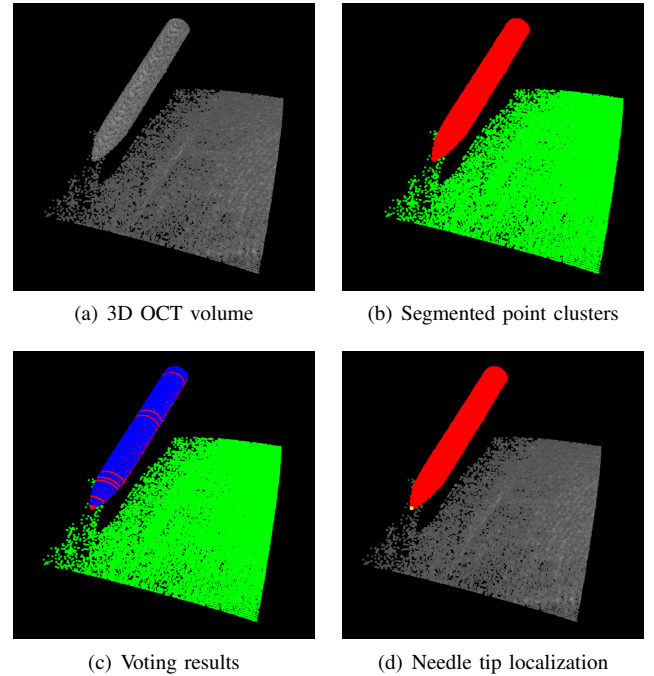


Fig. 5. (a) The needle with ex-vivo pig eye tissue in 3D OCT volume. (b) The points are clustered and marked with different colors. (c) 2D Detected ellipses from Fig. 4(b) are colored in blue and used for voting. (d) Needle segmentation and needle tip localization (the needle tip is marked by a yellow point).

C. Hand-eye calibration

The hand-eye calibration is usually defined by solving a system of homogeneous matrix equations in the form $AX = ZB$, where X and Z are rigid transformations defined by the configuration used. The calibration usually involves eye-in-hand and eye-to-hand configurations. The camera is said to be eye-in-hand when rigidly mounted on the robot end-effector,

Algorithm 1 Segmentation of needle body in 3D

INPUT: C - Euclidean point clusters $\{(c_1)\dots(c_n)\}$
OUTPUT: c_i - Cluster with the greatest number of votes

```

1: procedure SEGMENTNEEDLE( $C$ )
2:    $maxVote = 0, maxIndex = 0, vote = 0$ 
3:   for each cluster  $i$  in  $C$  do
4:     for each point  $j$  in  $i$  do
5:       if  $b_j == 1$  then
6:          $vote = vote + 1$ 
7:       end if
8:     end for
9:     if  $vote > maxVote$  then
10:       $maxVote = vote$ 
11:       $maxIndex = i$ 
12:    end if
13:   $vote = 0$ 
14: end for
15:  Return  $C(maxIndex)$ 
16: end procedure

```

and it is said to be eye-to-hand when it observes the robot within its work space. The latter is our setup, and since our needle is attached directly to the end effector of the robot, and given the unique kinematics of the robot [18], we can find $A' = AX$. We then move the robot with micro-scale displacements and formulate the system as follows:

$$\begin{bmatrix} A'_i \\ \vdots \\ A'_j \end{bmatrix} = [R \quad | \quad T] \times \begin{bmatrix} B_i \\ \vdots \\ B_j \end{bmatrix} \quad (3)$$

where $A' = \{A'_i, \dots, A'_j\}$ is the 3D needle position in the robot coordinate system and $B = \{B_i, \dots, B_j\}$ is the corresponding needle position in the camera coordinate system. $R \in SO_3$ and $T \in \mathbb{R}^3$ are the rotation matrix and translation vector that transform the needle positions from the OCT camera coordinate system to the robot coordinate system. The transformation matrix is represented as,

$$[R \quad | \quad T] = \begin{bmatrix} R_{3 \times 3} & T_{3 \times 1} \\ 0_{1 \times 3} & 1 \end{bmatrix} \quad (4)$$

We apply two different methods to solve Eqn. 3: in the first method (SVD), we calculate the rotation and translation parameters separately based on singular value decomposition [32]; and in the second method (QT), we use unit quaternions [33]. A linear Kalman filter [34] can be used on the needle tip position, for noise reduction, before passing it to either one of the above methods. This filter can predict the future state of a system, so it is very useful for the prediction of the position of the needle.

IV. EXPERIMENT

The experimental setup with an ex-vivo pig eye is depicted in Fig. 6. The OPMI LUMERA 700, with integrated RESCAN 700 OCT engine, is fixed on the optical table to reduce the influence of ambient vibration. The *CALLISTO* eye assistance computer system (Carl Zeiss Meditec AG., Germany) is utilized to simultaneously display the microscopic (en-face) image and B-scan images. The iRAM!S eye surgical robot

with 5 DoF is mounted on the adjusted bracket. Piezo motors (SmarACT GmbH, Germany), used in the robot, provide 1 μ m of accuracy using PID control with integrated incremental optical encoders. A 30G needle, typical for ophthalmic injection with a diameter of 0.31mm, is mounted on the end effector of the robot. The needle tip is fixed in its initial position very close to the ex-vivo pig eye to simulate an ophthalmic operation. The ex-vivo pig eye is fixed with pins into a rubber support. The program is executed on the laptop with an Intel

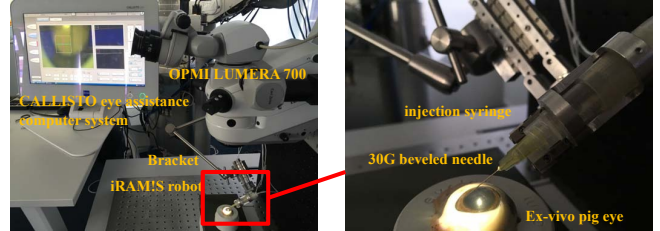


Fig. 6. The experimental setup for hand-eye calibration with ex-vivo pig eye.

Core i7 CPU in Ubuntu 16.04 with Point Cloud Library 1.8 and OpenCV 3.3 in C++.

We are aiming to intraoperatively calibrate the robot and OCT camera with micro-scale movements. In calibration trajectory #1, the needle is moved 10 steps, each being 20 μ m, first in the X-, then Z-, then Y- direction. Trajectory #2, is a zigzag, in which the needle moves 5 steps, each being 20 μ m, in the X-, Z- and Y- direction. The same trajectory is repeated once again. After each step is finished, the OCT engine is triggered in order to capture an image volume. The parameters for the OCT calibration are listed in Tab. I. These parameter were used to calculate the corrected needle tip position.

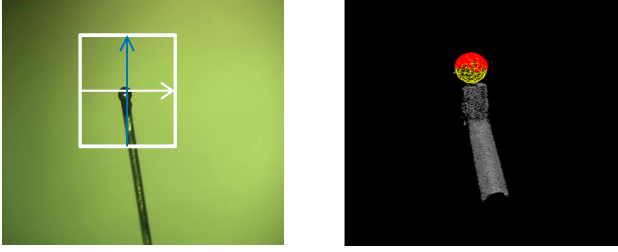
TABLE I
THE OCT CALIBRATION PARAMETERS (MM)

x_c	z_{xc}	y_c	z_{yc}
1.489	151.563	1.068	428.541

To evaluate the accuracy of our calibration method, we compared it with a reference method (marker-based). The reference method is created by attaching a 0.5mm diameter steel ball (Chrome AISI 52100 Grade 10) with a diameter accuracy of 2.5 μ m on the end of the needle. The steel ball has a half sphere surface in the OCT volume, which makes it detectable using RANSAC sphere fitting, see Fig. 7.

V. RESULTS

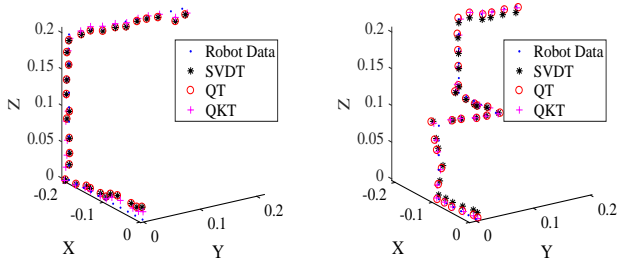
Fig. 8 and Fig. 9 show the trajectories of the marker based method and our proposed calibration method, respectively. The trajectories of both methods are transformed from the OCT coordinate system to the robot coordinate system with a transformation matrix derived from the methods described in Section III-C: SVD, QT and quaternion method with linear Kalman filter (QKT). As shown in the figures, all three methods resulted in a trajectory that overall fits well with the trajectory in the robot coordinate system (i.e Robot Data in Fig. 8 and Fig. 9), even though some outliers exist. The average computation time for detecting and transforming one



(a) The ball marker in microscopic view (b) The ball marker detected in 3D view

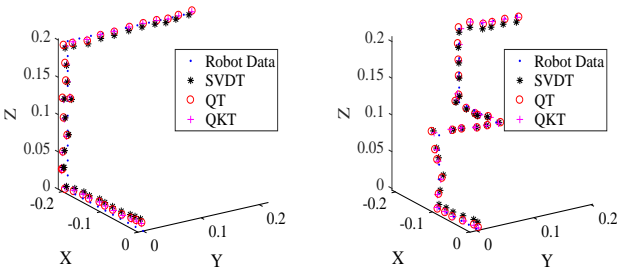
Fig. 7. The steel ball attached to the tool tip in microscopic image (a) and the detected steel ball in 3D OCT volume using RANSAC sphere fitting (b).

marker ball center and one needle tip position is 1.5s and 0.6s, respectively.



(a) Trajectory#1 of marker ball center (b) Trajectory#2 of marker ball center

Fig. 8. The marker ball center trajectory#1 (a) and trajectory#2 (b) in robot coordinate system and the data points transformed from OCT volumes using QT, SVDT, and QKT.



(a) Trajectory#1 of needle tip (b) Trajectory#2 of needle tip

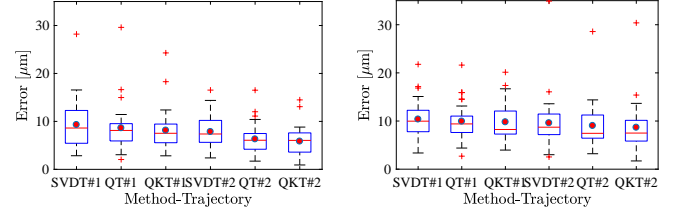
Fig. 9. The needle tip trajectory#1 (a) and trajectory#2 (b) in robot coordinate system and the data points transformed from OCT volumes using QT, SVDT, and QKT.

The calibration error for a point is calculated as,

$$e_i = \sqrt{(x_i^R - x_i^{R'})^2 + (y_i^R - y_i^{R'})^2 + (z_i^R - z_i^{R'})^2} \quad (5)$$

where (x_i^R, y_i^R, z_i^R) is the (needle tip/marker ball center) position in the robot coordinate system and $(x_i^{R'}, y_i^{R'}, z_i^{R'})$ is the (needle tip/marker ball center) transformed from the OCT coordinate system.

Fig. 10 gives the error e with box-and-whisker plots for each method and trajectory. The maximum whisker length is specified as 1.0 times of the interquartile range. Data points

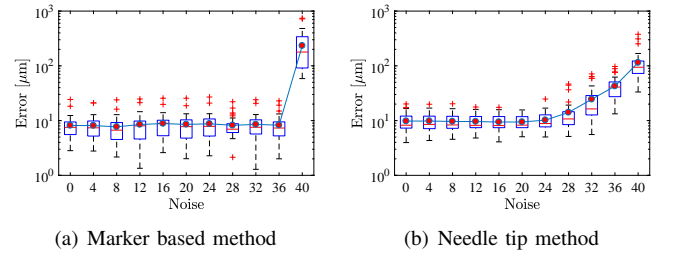


(a) Marker ball calibration error

(b) Needle tip calibration error

Fig. 10. The calibration error for two trajectories with each method using steel ball(a) and needle tip (b).

beyond the whiskers are treated as outliers. The whiskers are showing the minimum and maximum recorded error while the first (25%) and third (75%) quartile are shown at the bottom and top edge of the box. Bands and red dots represent the median and the mean of the error data, respectively. From the figure, we can see that all the methods maintain a low error without a significant difference. For the marker based method, QKT outperforms SVDT & QT slightly, with an average error of 0.8 μm and 1.2 μm for trajectory#1 and #2, respectively. For the needle tip method (i.e our proposed method), QKT outperforms the other two methods slightly with an average error of 0.4 μm and 0.6 μm for trajectory#1 and #2, respectively. It also shows that the performance gap between the marker based method and the needle tip method is very small with an average error of 7.0 μm and 9.2 μm , respectively.



(a) Marker based method

(b) Needle tip method

Fig. 11. The relationship between the calibration error for each point and standard deviation sigma of the Gaussian noise for marker based method (a) and needle tip based method (b).

In order to test the robustness of the proposed method, we carry out a noise test for the QKT method (i.e. method with the best error), trajectory#1. A zero-mean Gaussian noise is added to each B-scan image from standard deviation $\sigma = 0$ to $\sigma = 40$ by steps of 4. The relationship between the calibration error and the degree of noise added for both methods is shown in Fig. 11. We can see that the error for the marker based method (Fig. 11(a)) remains stable before $\sigma = 36$, but changes dramatically for $\sigma = 40$. This is due to the fact, that with too much noise added in the image, the sphere fitting cannot work correctly. For the needle tip method (Fig. 11(b)), the error remains stable before $\sigma = 24$, and steadily increases with more noise. This is because we are detecting shifted versions of the actual needle, due to the noise attached to the tip. From the above results, we find that our proposed method shows a suitable accuracy performance within a clinical tolerance. The method also showed robustness to noise influence.

VI. CONCLUSION&DISCUSSION

We proposed a flexible framework for calibrating an ophthalmic robot with an intra-operative MI-OCT. No markers were introduced in the calibration process, which makes our method easier to integrate into the current operation room, by avoiding instrument modification and sterilization. The calibration error of 9.2 μm meets the requirement of ophthalmic operations. Although micron-level displacements in the calibration process may cause safety concerns, the relative position between needle tip and eye tissue surface can be estimated to ensure safety. Accordingly, systems-theoretic safety assessments [35] could be a potential path for completing, refining, adapting, and customizing the whole setup and framework.

In future work, besides the needle tip information, the extra geometric constraints from the needle [28] or even the full geometric information of needle (i.e. CAD model of the needle) could be a potential improvement to increase the accuracy and robustness of the method. Nevertheless, this paper firstly verify the feasibility and accuracy performance of hand-eye calibration between OCT camera and ophthalmic robot, which motivates future work of path planning for ophthalmic injection and OCT based visual servoing control to achieve an enhanced RAS.

REFERENCES

- [1] T. Nakano, N. Sugita, T. Ueta, Y. Tamaki, and M. Mitsuishi, "A parallel robot to assist vitreoretinal surgery," *Int. J. Comput. Assist. Radiol. Surg.*, vol. 4, no. 6, pp. 517–526, 2009.
- [2] W. T. Ang, C. N. Riviere, and P. K. Khosla, "Design and implementation of active error canceling in hand-held microsurgical instrument," in *Intelligent Robot. Syst. 2001 IEEE/RSJ Int. Conf.*, vol. 2. IEEE, 2001, pp. 1106–1111.
- [3] W. Wei, R. Goldman, N. Simaan, H. Fine, and S. Chang, "Design and theoretical evaluation of micro-surgical manipulators for orbital manipulation and intraocular dexterity," in *Robot. Autom. 2007 IEEE Int. Conf.* IEEE, 2007, pp. 3389–3395.
- [4] R. Taylor, P. Jensen, L. Whitcomb, A. Barnes, R. Kumar, D. Stoianovici, P. Gupta, Z. Wang, E. Dejuan, and L. Kavoussi, "A steady-hand robotic system for microsurgical augmentation," *Int. J. Rob. Res.*, vol. 18, no. 12, pp. 1201–1210, 1999.
- [5] F. Ullrich, C. Bergeles, J. Pokki, O. Ergeneman, S. Erni, G. Chatzipirpiridis, S. Pané, C. Framme, and B. J. Nelson, "Mobility experiments with microrobots for minimally invasive intraocular SurgeryMicrorobot experiments for intraocular surgery," *Invest. Ophthalmol. Vis. Sci.*, vol. 54, no. 4, pp. 2853–2863, 2013.
- [6] H. C. M. Meenink, R. Rosielle, M. Steinbuch, H. Nijmeijer, and M. C. De Smet, "A master-slave robot for vitreo-retinal eye surgery," in *Euspen Int. Conf.*, 2010, pp. 3–6.
- [7] E. Rahimy, J. Wilson, T. C. Tsao, S. Schwartz, and J. P. Hubschman, "Robot-assisted intraocular surgery: development of the IRISS and feasibility studies in an animal model," *Eye*, vol. 27, no. 8, pp. 972–978, 2013.
- [8] C. Song, P. L. Gehlbach, and J. U. Kang, "Active tremor cancellation by a smart handheld vitreoretinal microsurgical tool using swept source optical coherence tomography," *Opt. Express*, vol. 20, no. 21, pp. 23 414–23 421, 2012.
- [9] M. A. Nasser, M. Eder, S. Nair, E. C. Dean, M. Maier, D. Zapp, C. P. Lohmann, and A. Knoll, "The introduction of a new robot for assistance in ophthalmic surgery," in *Eng. Med. Biol. Soc. (EMBC), 2013 35th Annu. Int. Conf. IEEE*. IEEE, 2013, pp. 5682–5685.
- [10] A. Gijbels, E. Vander Poorten, B. Gorissen, A. Devreker, P. Stalmans, and D. Reynaerts, "Experimental validation of a robotic comanipulation and telemanipulation system for retinal surgery," in *2014 5th IEEE RAS EMBS Int. Conf. Biomed. Robot. Biomechatronics*. IEEE, 2014, pp. 144–150.
- [11] T. Meenink, G. Naus, M. de Smet, M. Beelen, and M. Steinbuch, "Robot assistance for micrometer precision in vitreoretinal surgery," *Investig. Ophthalmol. & Vis. Sci.*, vol. 54, no. 15, p. 5808, 2013.
- [12] B. Gonenc, A. Chamani, J. Handa, P. Gehlbach, R. H. Taylor, and I. Iordachita, "3-DOF Force-Sensing Motorized Micro-Forceps for Robot-Assisted Vitreoretinal Surgery," *Sensors*, vol. 17, no. 11, pp. 3526–3541, 2017.
- [13] D. Huang, E. A. Swanson, C. P. Lin, J. S. Schuman, W. G. Stinson, W. Chang, M. R. Hee, T. Flotte, K. Gregory, C. A. Puliafito, and J. G. Fujimoto, "Optical coherence tomography," *Science (New York, NY)*, vol. 254, no. 5035, p. 1178, 1991.
- [14] T. Probst, K.-K. Maninis, A. Chhatkuli, M. Ourak, E. Vander Poorten, and L. Van Gool, "Automatic tool landmark detection for stereo vision in robot-assisted retinal surgery," *IEEE Robotics and Automation Letters*, vol. 3, no. 1, pp. 612–619, 2018.
- [15] J. P. Ehlers, P. K. Kaiser, and S. K. Srivastava, "Intraoperative optical coherence tomography using the RESCAN 700: preliminary results from the DISCOVER study," *Br. J. Ophthalmol.*, pp. 1329–1332, 2014.
- [16] J. D. Díaz, D. Kundrat, K.-F. Goh, O. Majdani, and T. Ortmaier, "Towards intra-operative oct guidance for automatic head surgery: first experimental results," in *MICCAI*. Springer, 2013, pp. 347–354.
- [17] G.-W. Cheon, Y. Huang, and J. U. Kang, "Active depth-locking handheld micro-injector based on common-path swept source optical coherence tomography," in *SPIE BiOS*. International Society for Optics and Photonics, 2015, pp. 93 170U–93 170U.
- [18] M. Nasser, M. Maier, and C. Lohmann, "A targeted drug delivery platform for assisting retinal surgeons for treating age-related macular degeneration (amd)," in *Engineering in Medicine and Biology Society (EMBC), 2017 39th Annual International Conference of the IEEE*. IEEE, 2017, pp. 4333–4338.
- [19] R. Y. Tsai and R. K. Lenz, "A new technique for fully autonomous and efficient 3d robotics hand/eye calibration," *IEEE Transactions on robotics and automation*, vol. 5, no. 3, pp. 345–358, 1989.
- [20] É. Marchand, F. Spindler, and F. Chaumette, "Visp for visual servoing: a generic software platform with a wide class of robot control skills," *IEEE Robotics & Automation Magazine*, vol. 12, no. 4, pp. 40–52, 2005.
- [21] Y. C. Shiu and S. Ahmad, "Calibration of wrist-mounted robotic sensors by solving homogeneous transform equations of the form $ax = xb$," *IEEE Transactions on robotics and automation*, vol. 5, no. 1, pp. 16–29, 1989.
- [22] I. Morgan, U. Jayarathne, A. Rankin, T. M. Peters, and E. C. Chen, "Hand-eye calibration for surgical cameras: a procrustean perspective-n-point solution," *Int. J. Comput. Assist. Radiol. Surg.*, pp. 1–9, 2017.
- [23] S. Thompson, D. Stoyanov, C. Schneider, K. Gurusamy, S. Ourselin, B. Davidson, D. Hawkes, and M. J. Clarkson, "Hand-eye calibration for rigid laparoscopes using an invariant point," *Int. J. Comput. Assist. Radiol. Surg.*, vol. 11, no. 6, pp. 1071–1080, 2016.
- [24] C. Bergmeir, M. Seitel, C. Frank, R. De Simone, H.-P. Meinzer, and I. Wolf, "Comparing calibration approaches for 3d ultrasound probes," *Int. J. Comput. Assist. Radiol. Surg.*, vol. 4, no. 2, p. 203, 2009.
- [25] J. Sarrazin, E. Promayon, M. Baumann, and J. Troccaz, "Hand-eye calibration of a robot-ultrasound probe system without any 3d localizers," in *Engineering in Medicine and Biology Society (EMBC), 2015 37th Annual International Conference of the IEEE*. IEEE, 2015, pp. 21–24.
- [26] K. Pachtrachai, M. Allan, V. Pawar, S. Hailes, and D. Stoyanov, "Hand-eye calibration for robotic assisted minimally invasive surgery without a calibration object," in *Intelligent Robot. Syst. 2006 IEEE/RSJ Int. Conf. IEEE*, 2016, pp. 2485–2491.
- [27] F. Vasconcelos, D. Peebles, S. Ourselin, and D. Stoyanov, "Similarity registration problems for 2d/3d ultrasound calibration," in *European Conference on Computer Vision*. Springer, 2016, pp. 171–187.
- [28] —, "Spatial calibration of a 2d/3d ultrasound using a tracked needle," *Int. J. Comput. Assist. Radiol. Surg.*, vol. 11, no. 6, pp. 1091–1099, 2016.
- [29] C. N. Riviere and P. S. Jensen, "A study of instrument motion in retinal microsurgery," in *Eng. Med. Biol. Soc. (EMBC), 2000 22th Annu. Int. Conf. IEEE*, vol. 1. IEEE, 2000, pp. 59–60.
- [30] S. Van der Jeught, J. A. Buytaert, A. Bradu, A. G. Podoleanu, and J. J. Dirckx, "Real-time correction of geometric distortion artefacts in large-volume optical coherence tomography," *Measurement Science and Technology*, vol. 24, no. 5, p. 057001, 2013.
- [31] H. Roodaki, K. Filippatos, A. Eslami, and N. Navab, "Introducing Augmented Reality to Optical Coherence Tomography in Ophthalmic Microsurgery," in *Mix. Augment. Reality, 2015 IEEE Int. Symp.* IEEE, 2015, pp. 1–6.
- [32] K. Arun, T. Huang, and S. Blostein, "Least-squares fitting of two 3-d point sets," *IEEE Trans. Pattern Anal. Mah. Intell.*, vol. 9, no. 5, pp. 698–700, 1987.
- [33] B. K. P. Horn, "Closed-form solution of absolute orientation using unit quaternions," *Journal of the Optical Society of America A*, vol. 4, no. 4, pp. 629–642, 1987.
- [34] P. Chatelain, A. Krupa, and M. Marchal, "Real-time needle detection and tracking using a visually servoed 3d ultrasound probe," in *Robotics and*

Automation (ICRA), 2013 IEEE International Conference on. IEEE, 2013, pp. 1676–1681.

- [35] H. Alemzadeh, D. Chen, A. Lewis, Z. Kalbarczyk, J. Raman, N. Leveson, and R. Iyer, “Systems-theoretic safety assessment of robotic telesurgical systems,” in *Computer Safety, Reliability, and Security*. Springer International Publishing, 2015, pp. 213–227.